machines

MDPI

Article

Dynamic Modeling and Validation of Dual-Cable Double-Pendulum Systems for Gantry Cranes

Bowen Jin [1,†], Ji Zeng [2,*,†], Pan Gao [2], He Zhang [1] and Shenwei Ge [1]

[1] Merchant Marine College, Shanghai Maritime University, Shanghai 201308, China; 201940110017@stu.shmtu.edu.cn (B.J.); 201940110013@stu.shmtu.edu.cn (H.Z.); geshenwei@jssc.edu.cn (S.G.)
[2] College of Ocean Science and Engineering, Shanghai Maritime University, Shanghai 201308, China; pgao@shmtu.edu.cn
* Correspondence: zengji@shmtu.edu.cn
† These authors contributed equally to this work.

Abstract

This paper presents a novel dynamic modeling framework for gantry crane systems based on the cart double pendulum with dual cables (CDPD) model. The CDPD model systematically incorporates the effects of dual suspension cables, equalizer beams, and closed-chain kinematic constraints, enabling an accurate simulation of both symmetric and asymmetric lifting scenarios. Utilizing Kane's method, the model efficiently handles redundant coordinates and holonomic constraints, resulting in a compact and numerically robust formulation. Validation results demonstrate strict energy conservation and consistency with traditional models in limiting cases. The proposed approach provides a unified and extensible foundation for the advanced analysis, control, and optimization of large-scale gantry crane operations.

Keywords: dynamic modeling; double pendulum; dual cable; gantry crane; closed-loop kinematic chain; nonlinear system

check for updates

Academic Editor: Carmine Maria Pappalardo

Received: 13 June 2025
Revised: 20 July 2025
Accepted: 25 July 2025
Published: 1 August 2025

Citation: Jin, B.; Zeng, J.; Gao, P.; Zhang, H.; Ge, S. Dynamic Modeling and Validation of Dual-Cable Double-Pendulum Systems for Gantry Cranes. *Machines* **2025**, *13*, 676. https://doi.org/10.3390/machines13080676

Copyright: © 2025 by the authors. Licensee MDPI, Basel, Switzerland. This article is an open access article distributed under the terms and conditions of the Creative Commons Attribution (CC BY) license (https://creativecommons.org/licenses/by/4.0/).

1. Introduction

The lifting and transportation of large, heavy structures (see Figure 1) are pivotal operations in the shipbuilding sector, involving the movement of substantial hull sections, heavy electromechanical equipment, and pre-assembled modules. The multibody dynamic modeling of lifting systems has great significance for various aspects of system design, control, optimization, and safety analysis [1–4]. The escalating demand for intricate lifting operations in sectors such as shipbuilding, aerospace, and heavy engineering has made traditional simplified models insufficient to meet contemporary engineering standards for precision, reliability, and safety [5]. Consequently, researchers have refocused on the development of more advanced and precise modeling techniques [6–8]. The limitations inherent in conventional models, exemplified by the CP system [9], suggest a need for more sophisticated approaches [10,11]. For example, investigations using nonlinear models that incorporate CDP system dynamics have achieved significant advancements in control strategies and crane system design [12–17].

In contrast, research on multi-cable lifting systems remains relatively limited and merits additional exploration. In 2013, Maleki et al. first studied the dynamic behavior of a dual-hoist bridge crane [18]. Arena et al. investigated the dynamics of container cranes, focusing on three-dimensional modeling and full-scale experiments [19,20]. In 2015, Lu et al. established a single-crane dual-cable system using Lagrange's method [21] and

applied adaptive trajectory tracking control [22] and a nonlinear controller in 2018 [23]. In 2020, Lu et al. further developed a dual-overhead crane system using the TMT method and a high-performance nonlinear controller [24]. In 2022, Wen Tianci et al. proposed an adaptive SMC strategy based on neural networks [25]. In 2015, Leban et al. introduced an inverse kinematic control approach for a fixed dual-rotary crane system derived using Newton's second law [26]. In 2018, Fu et al. investigated a cooperative dual-rotary crane system [27]. In 2020, Sun et al. developed a dual-rotary crane system and applied a nonlinear motion controller [28,29]. In 2022, Liu et al. proposed a collaborative anti-swing hoisting control strategy [30]. In 2019, Zhao and Huang developed a dual-crane model that considers distributed mass loads using Lagrange's method [31]. In 2020, Huang and Zhu expanded this framework to encompass a three-dimensional dual-crane system using Kane's method [32]. The current developments of dual-crane systems have yielded notable advancements in simulations, control strategies, environmental response analysis, and the incorporation of artificial intelligence [23–25,29,30,32,33].



Figure 1. Schematic of a large-scale lifting operation in shipbuilding.

Meanwhile, large gantry crane systems employed in high-demand operations—such as in the handling of heavy and oversized loads—often call for the use of equalizer beams (see Figure 2) or other mechanisms to effectively distribute and balance the weight. These beams can significantly influence the dynamics and should not be overlooked. Despite this, a comprehensive dynamic model that integrates double-pendulum effects for multi-crane systems has yet to be established, highlighting a critical gap in previous research.

This paper introduces a novel modeling approach for large-scale gantry crane systems by developing a CDPD model. Unlike traditional models, the proposed method systematically incorporates both the double-pendulum effects and the closed-chain constraints arising from equalizer beams and dual suspension cables. Compared to existing double-pendulum or dual-cable models, this work advances the state of the art by (1) explicitly modeling the influence of equalizer beams and their mass distribution, which are often neglected but critical in heavy-duty lifting operations; (2) providing a unified framework that can degenerate to simpler models under symmetric or limiting conditions, thus ensuring broad applicability and consistency; and (3) enabling an analysis of asymmetric configurations, variable cable lengths, and inclined suspension scenarios that are challenging for conventional models.



Figure 2. Photograph of the main hooks and equalizer beams in a gantry crane system.

2. Methodology

2.1. Kane's Method for Multibody Dynamics

Kane's method is a powerful multibody dynamics analysis tool using generalized speeds and partial velocities to streamline the derivation of the dynamic equations. By transforming a set of second-order nonlinear equations into first-order linear equations, Kane's method significantly reduces the order and complexity of dynamical systems. In complex systems, it not only simplifies the derivation of the dynamic equations but also effectively manages redundant constraints, making it particularly suitable for closed-chain configurations. In contrast to traditional methods, such as Newtonian or Lagrangian approaches, which can involve lengthy derivations and high computational demands, Kane's method uses the orthogonality properties of partial velocities and generalized inertial forces to generate compact ODEs. This approach notably increases the efficiency and scalability of modeling high-dimensional systems [34–36].

In this study, the system under consideration is a CKC multibody structure [37–39]. It is necessary to transform the CKC configuration into a tree-structured system with full constraints and additional coordinates in order to model such a system. In the presence of holonomic constraints, the equations of motion consist of kinematic differential equations $\bar{f}_k = 0$, dynamic differential equations $\bar{f}_d = 0$, and holonomic constraint equations $\bar{f}_h = 0$ [40,41]. The system involves $N = n + s$ total coordinates, where $n = 4$ are generalized coordinates $\bar{q}$, and $s = 2$ are additional dependent coordinates $\bar{q}_r$. The holonomic constraint equations are expressed as

$$\bar{f}_h(\bar{q}, \bar{q}_r, t) = 0. \tag{1}$$

Similar to the coordinates, n generalized speeds u and s dependent speeds u_r are introduced through N kinematic differential equations:

$$\bar{f}_k(\dot{\bar{q}}, \dot{\bar{q}}_r, \bar{u}, \bar{u}_r, \bar{q}, \bar{q}_r, t) = 0. \tag{2}$$

The equations of motion are formulated by transforming the holonomic constraints into functions of the generalized speeds:

$$\bar{f}_{hs}(\bar{u}, \bar{u}_r, \bar{q}, \bar{q}_r, t) = \mathbf{M}_{hs}\bar{u}_r + \bar{g}_{hs} = 0. \tag{3}$$

By solving for the dependent generalized speeds, we obtain

$$\bar{u}_r = -\mathbf{M}_{hs}^{-1}\bar{g}_{hs}. \tag{4}$$

This allows us to rewrite the kinematic and dynamic differential equations in terms of the generalized speeds, their derivatives, the generalized coordinates, and the dependent coordinates:

$$\bar{f}_k(\dot{\bar{q}}, \dot{\bar{q}}_r, \bar{u}, \bar{q}, \bar{q}_r, t) = 0, \tag{5}$$

$$\bar{f}_d(\dot{\bar{u}}, \bar{u}, \bar{q}, \bar{q}_r, t) = 0. \tag{6}$$

Finally, by establishing the constraint equations $\bar{f}_h = 0$, kinematic equations $\bar{f}_k = 0$, and dynamics equations $\bar{f}_d = 0$, numerical integration can be performed to enable a simulation and analysis of the multibody system.

2.2. Modeling Assumptions

To facilitate analytical tractability and focus on the principal dynamic characteristics of the system, the following standard modeling assumptions are adopted:

- **Planar motion:** The analysis is limited to two-dimensional (planar) motion, and any out-of-plane dynamics are neglected. This is justified because heavy-duty crane operations typically separate motions in orthogonal directions, and lateral wind loads are not considered in this study.
- **Ideal joints and connections:** All joints and connections are modeled as perfect kinematic pairs. The influence of auxiliary mechanisms, such as pulleys within equalizer beams, is neglected.
- **Rigid bodies:** The crane carts, equalizer beams, and payload are treated as rigid bodies. The rotational inertia of point masses is ignored, and only translational dynamics are considered. Since the system studied in this paper operates at low speeds and rotational effects are even smaller, the influence of rotational inertia is neglected.
- **Cables:** All suspension cables are modeled as massless, inextensible, and always taut. This is justified for large-scale gantry cranes, where the cable mass is negligible relative to the payload and equalizer beams, and cable elasticity has minimal effect on the system dynamics of slow movements.
- **External disturbances:** Effects such as friction, aerodynamic forces, and mechanical vibrations are neglected. Only gravitational forces and the horizontal control force applied to the crane carts are included.

These assumptions enable a focused investigation of the dominant dynamic responses. The simulation framework, however, is designed to be extensible, allowing for the incorporation of additional environmental forces in future studies.

2.3. System Description

2.3.1. System Composition

Large gantry cranes for heavy and oversized lifting typically operate at low speeds but exhibit pronounced double-pendulum effects due to the significant mass of the hooks, equalizer beams, and auxiliary devices. These features introduce complex dynamic behaviors that must be accurately modeled for reliable simulation and analysis.

To address these challenges, this study develops a dynamic model for a dual-crane system that explicitly incorporates double-pendulum effects, improving fidelity and applicability for engineering applications involving large-scale hoisting.

As shown in Figure 3, the system is simplified into its essential components:

- **Carts:** Two movable bases traveling horizontally along rails, providing primary positioning.
- **Equalizer beams:** Devices suspended between the carts and payload to balance and distribute the load.
- **Payload:** The lifted object, typically large and heavy.
- **Cables:** Suspension elements connecting the carts, equalizer beams, and payload, forming the basis for double-pendulum dynamics.

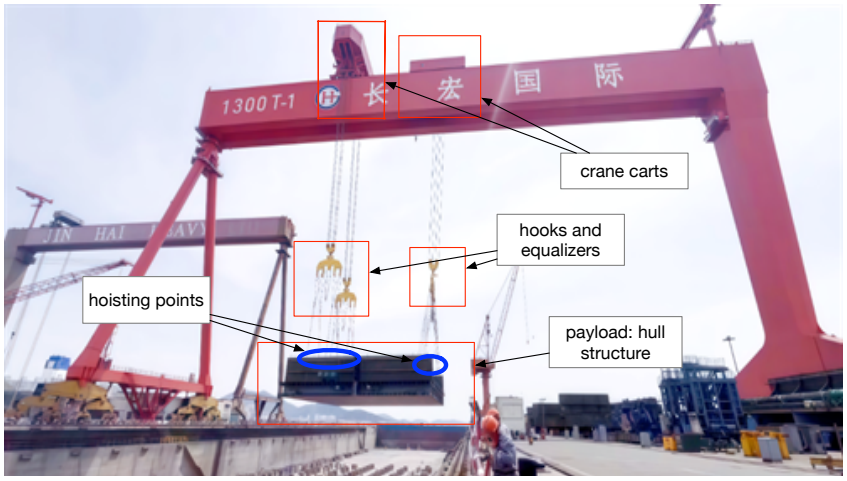


Figure 3. Schematic diagram of the main components of a gantry crane system.

Figure 4 illustrates the simplified gantry crane system used for analysis. Points 0 and 5 are the suspension points on the crane carts. Points 1 and 4 are the connection points for the equalizer beams, and Points 2 and 3 are the suspension points of the payload.

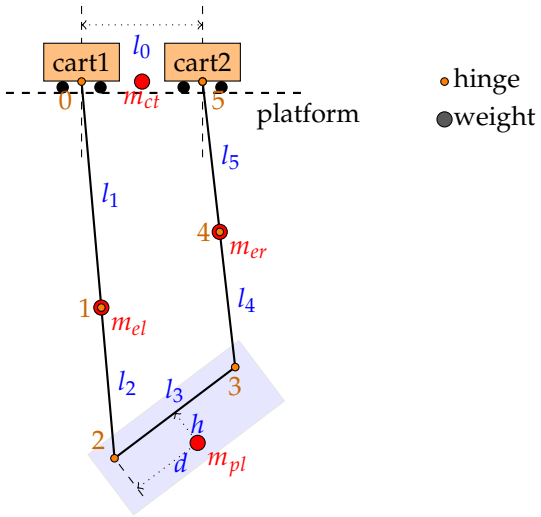


Figure 4. Schematic of the planar CDPD system.

The system consists of several main components. The crane carts, with total mass m_{ct}, move horizontally on a frictionless platform and are actuated by a control force F_C. The left and right equalizer beams are modeled as point masses m_{el} at Point 1 and m_{er} at Point 4,

respectively. The payload, with mass m_{pl}, is represented as a rigid rod between Points 2 and 3, with its center of gravity offset by d and h from Point 2.

This abstraction captures the essential double-pendulum dynamics while simplifying the system for analysis. It enables a focused study of the effects of mass distribution, cable tensions, and control forces on the overall dynamic response.

2.3.2. Mathematical Model and Coordinates

The CDPD system considered here is a CKC system, which presents greater modeling and computational challenges than tree-structured systems. To facilitate modeling, a common strategy is to temporarily "cut" a constraint, transforming the CKC into a tree structure, and then introduce constraint equations to maintain system integrity. In this work, the hinge at Point 5 is severed (see Figure 5), allowing the assignment of body-fixed coordinate systems to each rigid body for systematic analysis and mathematical formulation (Table 1).

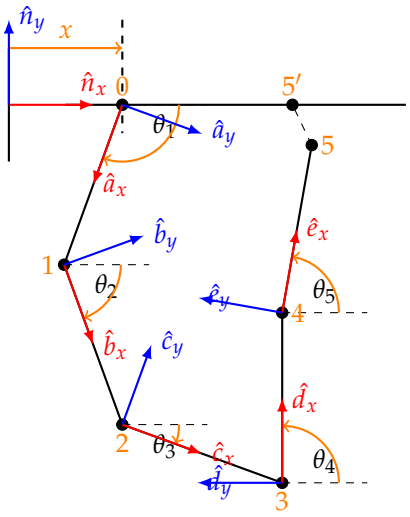


Figure 5. Mathematical model and coordinate systems for the CDPD system.

Table 1. Correspondence between coordinate systems and rigid bodies.

Coordinate System	Associated Body
N (inertial frame)	Ground (fixed reference)
A	Cart 1 to left equalizer beam (nodes 0–1)
B	Left equalizer beam to left hoisting point (nodes 1–2)
C	Payload (left to right hoisting points, nodes 2–3)
D	Right hoisting point to right equalizer beam (nodes 3–4)
E	Right equalizer beam to Cart 2 (nodes 4–5)

Note: Each body-fixed coordinate system is attached to its respective rigid body, as illustrated in Figure 5.

Each rigid body is assigned a body-fixed coordinate system, denoted by uppercase letters (A, B, C, D, and E), while the inertial (ground) frame is denoted by N. The unit vectors of the inertial frame N are defined as

$$\hat{I}_N = \begin{bmatrix} \hat{n}_x \\ \hat{n}_y \end{bmatrix}, \tag{7}$$

where $\hat{n}_x$ and $\hat{n}_y$ represent the x- and y-axis unit vectors, respectively.

Similarly, the unit vectors for the body-fixed frames are given by

$$\hat{I}_A = \begin{bmatrix} \hat{a}_x \\ \hat{a}_y \end{bmatrix}, \quad \hat{I}_B = \begin{bmatrix} \hat{b}_x \\ \hat{b}_y \end{bmatrix}, \quad \hat{I}_C = \begin{bmatrix} \hat{c}_x \\ \hat{c}_y \end{bmatrix}, \tag{8}$$

$$\hat{I}_D = \begin{bmatrix} \hat{d}_x \\ \hat{d}_y \end{bmatrix}, \quad \hat{I}_E = \begin{bmatrix} \hat{e}_x \\ \hat{e}_y \end{bmatrix}. \tag{9}$$

The position vectors of each node i are summarized in Table 2, where the subscript of $\bar{r}_i$ corresponds to the node numbering in the system, as illustrated in Figure 5.

Table 2. Physical meaning and expressions of position vectors ($\bar{r}_0$) to ($\bar{r}_5$).

Node	Physical Meaning	Position Vector Expression
$\bar{r}_0 = \bar{r}_{ct}$	Cart 1 position (left cart)	$x\,\hat{n}_x$
$\bar{r}_1 = \bar{r}_{el}$	Left equalizer beam	$x\,\hat{n}_x + l_1\hat{a}_x$
$\bar{r}_2$	Left payload suspension point	$x\,\hat{n}_x + l_1\hat{a}_x + l_2\hat{b}_x$
$\bar{r}_3$	Right payload suspension point	$x\,\hat{n}_x + l_1\hat{a}_x + l_2\hat{b}_x + l_3\hat{c}_x$
$\bar{r}_4 = \bar{r}_{er}$	Right equalizer beam	$x\,\hat{n}_x + l_1\hat{a}_x + l_2\hat{b}_x + l_3\hat{c}_x + l_4\hat{d}_x$
$\bar{r}_5$	Cart 2 position (right cart)	$x\,\hat{n}_x + l_1\hat{a}_x + l_2\hat{b}_x + l_3\hat{c}_x + l_4\hat{d}_x + l_5\hat{e}_x$
$\bar{r}_{pl}$	the position of the payload's CoG	$\bar{r}_2 + d\,\hat{c}_x + h\,\hat{c}_y$

Note: x is the horizontal position of Cart 1; l_k is the length of the k-th link; $\hat{a}_x, \hat{b}_x, \hat{c}_x, \hat{d}_x, \hat{e}_x$ are the x-axis unit vectors of the respective body-fixed frames, as shown in Figure 5.

Unlike many simplified models, this formulation does not assume a symmetric payload. The payload's CoG may be offset from the geometric center, as shown in Figure 4. The parameters d and h represent the horizontal and vertical offsets of the payload's CoG relative to node 2. This allows the model to handle both symmetric and asymmetric payloads, accommodating real-world irregularities and non-uniform mass distributions.

The CoG offset is explicitly included in the equations of motion. For example, the position of the payload's CoG is

$$\bar{r}_{pl} = \bar{r}_2 + d\,\hat{c}_x + h\,\hat{c}_y, \tag{10}$$

where $\hat{c}_x$ and $\hat{c}_y$ are the unit vectors of the payload-fixed frame.

For explicit coordinates, the position vector of each node is

$$\bar{r}_i = \left(x + \sum_{k=1}^{i} l_k \cos(\theta_k) \right) \hat{n}_x + \left(\sum_{k=1}^{i} l_k \sin(\theta_k) \right) \hat{n}_y, \tag{11}$$

where $i = 1, 2, 3, 4, 5$, and $\bar{r}_0 = x\hat{n}_x$. Here, x is the position of cart 1, and θ_i is the absolute angle of the i-th link. The parameters used are listed in Table 3.

Table 3. Main parameters used in the CDPD model.

Symbol	Description	Unit/Value
x	Horizontal position of cart 1 (left cart)	m
l_0	Distance between carts (platform length)	m
l_1	Length of left upper cable	m
l_2	Length of left lower cable	m
l_3	Length between payload suspension points	m
l_4	Length of right lower cable	m
l_5	Length of right upper cable	m

Table 3. *Cont.*

Symbol	Description	Unit/Value
d	Horizontal offset of payload CoG from node 2	m
h	Vertical offset of payload CoG from node 2	m
m_{ct}	Mass of crane carts (total)	ton or kg
m_{el}	Mass of left equalizer beam	ton or kg
m_{er}	Mass of right equalizer beam	ton or kg
m_{pl}	Mass of payload	ton or kg
F_C	Horizontal control force on cart(s)	N
g	Gravitational acceleration	$9.81\,\mathrm{m/s^2}$
θ_i	Absolute angle of the i-th link	rad or deg ($i = 1, \ldots, 5$)
u_x	Generalized speed of cart 1 (horizontal)	m/s
u_i	Generalized speed of the i-th link	m/s ($i = 1, \ldots, 5$)
T_i	Tension in the i-th cable	N ($i = 1, 2, 4, 5$)

Note: m denotes meters; *N* denotes newtons.

3. Dynamic Formulation

The dynamic behavior of the gantry crane system is formulated using Kane's method. This approach models the CKC multibody system with holonomic constraints, providing an accurate and systematic description of its kinematics, dynamics, and inter-component interactions.

3.1. Kinematic Equations

In contrast to the Lagrange method, Kane's method, after determining the generalized coordinates, requires the additional selection of generalized speeds. In the majority of cases, generalized speeds can be directly chosen as the derivatives of the generalized coordinates, providing a straightforward and unambiguous approach. Nevertheless, this approach does not fully leverage the advantage of Kane's method, as it may limit the flexibility of the dynamic model, particularly in systems where specific translational or rotational behaviors are of interest. Engineers are typically more interested in the horizontal linear velocity and acceleration of the payload in lifting systems. Hence, the generalized speeds that follow are used to describe the system's motion. The relationships between the generalized speeds $u_x, u_1, u_2, u_3, u_4, u_5$ and the derivatives of the generalized coordinates $\dot{x}$ and $\dot{\theta}_i$ are given as follows:

$$\dot{x} = u_x, \tag{12}$$

$$\dot{\theta}_i = \frac{u_i}{l_i} \quad (i = 1, 2, 3, 4, 5), \tag{13}$$

where u_i represents the linear velocity of every rotational component relative to its pivot, facilitating a straightforward calculation of the horizontal motion for every component in the lifting system.

In this study, $q_i,\ (i = 1, 2, 3, 4, 5)$ are angular displacement variables corresponding to $\theta_i,\ (i = 1, 2, 3, 4, 5)$, with their derivatives $\dot{\theta}_i$ representing the angular velocities. According to Equation (13), the chosen generalized speeds describe the linear velocities at specific nodes; for example, u_1 describes the linear velocity of node 1 relative to node 0 during circular motion. Under typical operating conditions of the lifting system, this mainly describes the horizontal relative motion speed of every node. This choice facilitates a more straightforward analysis of the horizontal motion of the payload, providing a clearer physical meaning. In engineering practice, linear velocities are often more intuitive than angular velocities, as they allow for a more direct visualization of the actual speed of every point. Based on this, the kinematic equations are established, and the system is rewritten in matrix form as follows:

$$\bar{f}_k = \mathbf{M_k}\dot{\bar{q}}_N + \bar{g}_k = 0, \tag{14}$$

where

$$\mathbf{M_k} = \begin{bmatrix} 1 & 0 & 0 & 0 & 0 & 0 \\ 0 & l_1 & 0 & 0 & 0 & 0 \\ 0 & 0 & l_2 & 0 & 0 & 0 \\ 0 & 0 & 0 & l_3 & 0 & 0 \\ 0 & 0 & 0 & 0 & l_4 & 0 \\ 0 & 0 & 0 & 0 & 0 & l_5 \end{bmatrix}, \dot{\bar{q}}_N = \begin{bmatrix} \dot{x} \\ \dot{\theta}_1 \\ \dot{\theta}_2 \\ \dot{\theta}_3 \\ \dot{\theta}_4 \\ \dot{\theta}_5 \end{bmatrix}, \bar{g}_k = \begin{bmatrix} -u_x \\ -u_1 \\ -u_2 \\ -u_3 \\ -u_4 \\ -u_5 \end{bmatrix}. \tag{15}$$

3.2. Holonomic Constraints

The crane system modeled in this study is a holonomic system with redundant coordinates, forming a CKC system with four degrees of freedom. Although six generalized coordinates are used to describe the system, only four are independent; the remaining two are redundant and must satisfy holonomic constraint equations.

To ensure that the system motion remains consistent with the closed-chain structure, constraint equations are imposed on the dependent generalized coordinates. As illustrated in Figure 5, nodes 5 and 5′ must coincide, leading to the following holonomic constraint equations:

$$\bar{f}_h = \begin{bmatrix} -l_0 + \sum_{k=1}^{5} l_k \cos(\theta_k) \\ \sum_{k=1}^{5} l_k \sin(\theta_k) \end{bmatrix} = 0. \tag{16}$$

Including these constraint equations in the simulation ensures that the system motion always satisfies the closed-chain requirements, correcting any errors introduced by the temporary severing of the chain for modeling purposes.

Differentiating the position constraint equations with respect to time yields the velocity-level (Pfaffian) constraints:

$$\dot{\bar{f}}_h = \begin{bmatrix} -\sum_{k=1}^{5} l_k \sin(\theta_k)\dot{\theta}_k \\ \sum_{k=1}^{5} l_k \cos(\theta_k)\dot{\theta}_k \end{bmatrix} = 0. \tag{17}$$

Substituting the generalized speed definitions ($\dot{\theta}_k = u_k/l_k$) into the above yields a linear relationship among the generalized speeds:

$$\bar{f}_{hs} = \begin{bmatrix} -\sum_{k=1}^{5} u_k \sin(\theta_k) \\ \sum_{k=1}^{5} u_k \cos(\theta_k) \end{bmatrix} = 0. \tag{18}$$

Solving these equations for the dependent generalized speeds (here, u_3 and u_4) in terms of the independent speeds (u_1, u_2, u_5) gives

$$u_3 = \frac{-u_1 \sin(\theta_1 - \theta_4) - u_2 \sin(\theta_2 - \theta_4) - u_5 \sin(\theta_5 - \theta_4)}{\sin(\theta_3 - \theta_4)}, \tag{19}$$

$$u_4 = \frac{u_1 \sin(\theta_1 - \theta_3) + u_2 \sin(\theta_2 - \theta_3) + u_5 \sin(\theta_5 - \theta_3)}{\sin(\theta_3 - \theta_4)}. \tag{20}$$

These expressions for the dependent generalized speeds are substituted into the kinematic ($\bar{f}_k$) and dynamic ($\bar{f}_d$) equations, ensuring that the overall system dynamics respect the holonomic constraints at all times.

3.3. Partial Velocity Matrix

The partial velocity matrix for the system is computed with regard to the independent generalized speeds, enabling the calculation of generalized forces and generalized inertial forces in the directions of these independent speeds. This matrix also serves as the foundation for analyzing the effect of generalized speed variations on every mass point within the

system. The partial velocities show how a given velocity or angular velocity will vary if one of the generalized speeds changes.

$$ {}^{N}\bar{v}_{ct}^{\bar{u}} = \begin{bmatrix} \hat{n}_x \\ 0 \\ 0 \\ 0 \end{bmatrix}. \tag{21} $$

The vector ${}^{N}\bar{v}_{ct}^{\bar{u}}$ represents the velocity of the crane cart relative to the inertial frame N, expressed in the generalized speed $\bar{u}$ space. It indicates that the velocity of the crane carts depends solely on the generalized speed u_x and is independent of other generalized speeds (such as u_1, u_2, and u_5).

For the motion of the crane cart governed by u_x, the velocities of the left and right equalizer beams, influenced by additional generalized speeds, are described as follows:

$$ {}^{N}\bar{v}_{el}^{\bar{u}} = \begin{bmatrix} \hat{n}_x \\ -\sin\theta_1\hat{n}_x + \cos\theta_1\hat{n}_y \\ 0 \\ 0 \end{bmatrix}, \tag{22} $$

The motion of the left equalizer is jointly controlled by u_x and u_1 and θ_1.

$$ {}^{N}\bar{v}_{er}^{\bar{u}} = \begin{bmatrix} \hat{n}_x \\ 0 \\ 0 \\ \sin\theta_5\hat{n}_x - \cos\theta_5\hat{n}_y \end{bmatrix}. \tag{23} $$

The motion of the right equalizer is determined by u_x and u_5 and θ_5.

$$ {}^{N}\bar{v}_{pl}^{\bar{u}} = \begin{bmatrix} \hat{n}_x \\ (\frac{d\sin(\theta_1-\theta_4)\sin\theta_3}{l_3\sin(\theta_3-\theta_4)} + \frac{h\sin(\theta_1-\theta_4)\cos\theta_3}{l_3\sin(\theta_3-\theta_4)} - \sin\theta_1)\hat{n}_x + (-\frac{d\sin(\theta_1-\theta_4)\cos\theta_3}{l_3\sin(\theta_3-\theta_4)} + \frac{h\sin(\theta_1-\theta_4)\sin\theta_3}{l_3\sin(\theta_3-\theta_4)} + \cos\theta_1)\hat{n}_y \\ (\frac{d\sin(\theta_2-\theta_4)\sin\theta_3}{l_3\sin(\theta_3-\theta_4)} + \frac{h\sin(\theta_2-\theta_4)\cos\theta_3}{l_3\sin(\theta_3-\theta_4)} - \sin\theta_2)\hat{n}_x + (-\frac{d\sin(\theta_2-\theta_4)\cos\theta_3}{l_3\sin(\theta_3-\theta_4)} + \frac{h\sin(\theta_2-\theta_4)\sin\theta_3}{l_3\sin(\theta_3-\theta_4)} + \cos\theta_2)\hat{n}_y \\ -\frac{(d\sin\theta_3+h\cos\theta_3)\sin(\theta_4-\theta_5)}{l_3\sin(\theta_3-\theta_4)}\hat{n}_x + \frac{(d\cos\theta_3-h\sin\theta_3)\sin(\theta_4-\theta_5)}{l_3\sin(\theta_3-\theta_4)}\hat{n}_y \end{bmatrix}. \tag{24} $$

For the payload, its motion is governed by all the generalized speeds: u_x, u_1, u_2, and u_5.

The relative angles $(\theta_1, \theta_2, \theta_5)$ define the orientation and swing of the payload. These angles interact with d and h to determine the precise position and trajectory of the payload's CoG.

By considering all these factors, the model captures the complex interplay of the linear and rotational dynamics affecting the payload, providing a comprehensive framework for analyzing its motion.

These equations highlight how the generalized speeds (u_x, u_1, u_2, u_5) and the angles $(\theta_1, \theta_2, \theta_3, \theta_4, \theta_5)$ collectively influence the dynamic behavior of the system. The partial velocity matrix $\mathbf{P_u}$ can then be defined as

$$ \mathbf{P_u} = \begin{bmatrix} {}^{N}\bar{v}_{ct}^{\bar{u}} & {}^{N}\bar{v}_{el}^{\bar{u}} & {}^{N}\bar{v}_{pl}^{\bar{u}} & {}^{N}\bar{v}_{er}^{\bar{u}} \end{bmatrix}. \tag{25} $$

3.4. Dynamic Equations

In Kane's method, the dynamic equations are derived based on the balance between generalized inertial forces and generalized active forces. According to Kane's principles, the sum of generalized inertial forces and generalized active forces must equal zero. Kane's method achieves this balance by ensuring that every generalized force component aligns

with a corresponding partial velocity, thus simplifying the projection of forces into the generalized coordinate space and reducing the computational complexity.

For the crane cart, a horizontal control force $F_C(t)$ is applied, directed to the right, along with the gravitational force acting on the cart:

$$\bar{F}_{ct} = F_C(t)\hat{n}_x - m_{ct}g\hat{n}_y, \tag{26}$$

$$\bar{F}_{el} = -m_{el}g\hat{n}_y, \tag{27}$$

$$\bar{F}_{er} = -m_{er}g\hat{n}_y, \tag{28}$$

$$\bar{F}_{pl} = -m_{p}g\hat{n}_y. \tag{29}$$

In practical engineering applications, these environmental forces play a significant role in system performance and safety. The model is extensible: additional force terms can be appended to the active force vectors $\bar{F}_{ct}$, $\bar{F}_{el}$, $\bar{F}_{er}$, and $\bar{F}_{pl}$ as required for a more realistic simulation or control design. For example, to include a wind load acting on the payload, simply add a wind force term F_{Wind} to $\bar{F}_{pl}$:

$$\bar{F}_{pl} = -m_{p}g\hat{n}_y + F_{\text{Wind}}, \tag{30}$$

where F_{Wind} is the wind force vector (e.g., $F_{\text{Wind}} = F_w\hat{n}_x$ for a horizontal wind load of magnitude F_w). This approach allows the model to account for wind disturbances or other external forces as needed.

The generalized active force F_A represents the projection of every object's active force into the generalized speed space:

$$F_A = \mathbf{P_u}\begin{bmatrix}\bar{F}_{ct}\\ \bar{F}_{el}\\ \bar{F}_{pl}\\ \bar{F}_{er}\end{bmatrix}, \tag{31}$$

$$F_A = \begin{bmatrix} F_C \\ \frac{dgm_p\sin(\theta_1-\theta_4)\cos(\theta_3)}{l_3\sin(\theta_3-\theta_4)} - \frac{ghm_p\sin(\theta_1-\theta_4)\sin(\theta_3)}{l_3\sin(\theta_3-\theta_4)} - gm_p\cos(\theta_1) - gm_{el}\cos(\theta_1) \\ \frac{dgm_p\sin(\theta_2-\theta_4)\cos(\theta_3)}{l_3\sin(\theta_3-\theta_4)} - \frac{ghm_p\sin(\theta_2-\theta_4)\sin(\theta_3)}{l_3\sin(\theta_3-\theta_4)} - gm_p\cos(\theta_2) \\ -\frac{dgm_p\sin(\theta_4-\theta_5)\cos(\theta_3)}{l_3\sin(\theta_3-\theta_4)} + \frac{ghm_p\sin(\theta_4-\theta_5)\sin(\theta_3)}{l_3\sin(\theta_3-\theta_4)} + gm_{er}\cos\theta_5 \end{bmatrix}. \tag{32}$$

The generalized inertial forces are calculated by determining the d'Alembert inertial forces for every mass point (the product of mass and acceleration) and projecting them into the generalized speed space through the partial velocity matrix.

The inertial force for the crane carts is

$$\bar{G}_{ct} = -m_c\dot{u}_x\hat{n}_x, \tag{33}$$

where $\bar{G}_{ct}$ signifies the inertial force due to the linear acceleration of the cart, aligned with the cart's primary motion direction. For the left equalizer beam,

$$\bar{G}_{el} = -m_{el}\dot{u}_x\hat{n}_x + \frac{m_{el}u_1^2}{l_1}\hat{a}_x - m_{el}\dot{u}_1\hat{a}_y. \tag{34}$$

For the right equalizer beam,

$$\bar{G}_{er} = -m_{er}\dot{u}_x\hat{n}_x - \frac{m_{er}u_5^2}{l_5}\hat{e}_x + m_{er}\dot{u}_5\hat{e}_y. \tag{35}$$

For the payload,

$$\begin{aligned}\bar{G}_{pl} = & -m_p\dot{u}_x\hat{n}_x + \frac{m_p u_1^2}{l_1}\hat{a}_x - m_p\dot{u}_1\hat{a}_y + \frac{m_p u_2^2}{l_2}\hat{b}_x - m_p\dot{u}_2\hat{b}_y \\ & + m_p\left(\frac{du_3^2}{l_3^2} + \frac{h\dot{u}_3}{l_3}\right)\hat{c}_x - m_p\left(\frac{d\dot{u}_3}{l_3} - \frac{hu_3^2}{l_3^2}\right)\hat{c}_y.\end{aligned} \tag{36}$$

The substitution of $u_r = [u_3, u_4]^T$ and its derivative allows for a complete expression of the inertial forces. Nevertheless, the resulting expressions are extensive and not displayed here in full.

The generalized inertial force vector F_I is given by

$$F_I = \mathbf{P_u}\begin{bmatrix}\bar{G}_{ct}\\ \bar{G}_{el}\\ \bar{G}_{pl}\\ \bar{G}_{er}\end{bmatrix}. \tag{37}$$

According to Kane's method, the dynamic equations are formulated as

$$F_A + F_I = \bar{f}_d = 0. \tag{38}$$

This equation can be transformed into a system of equations in terms of the derivatives of the independent generalized speeds $\dot{u} = [\dot{u}_x, \dot{u}_1, \dot{u}_2, \dot{u}_5]^T$:

$$\bar{f}_d = \mathbf{M_d}\dot{u} + \bar{g}_d = 0. \tag{39}$$

4. Numerical Implementation

4.1. Simulation Framework

The simulation framework is modular, comprising parameter definition, state initialization, dynamics integration, and post-processing. The system structural parameters are encapsulated in P_0, and the initial states in X_0. Among the generalized coordinates $(q_1, q_2, q_3, q_4, q_5)$, three are independent, and two are dependent, determined by solving the holonomic constraints $\bar{f}_h$. The control force $F_C(t)$ and the environmental forces can be added as time-dependent, supporting complex dynamic simulations.

$$P_0 = \begin{bmatrix}l_0\\ l_1\\ l_2\\ l_3\\ l_4\\ l_5\\ d\\ h\\ m_{ct}\\ m_{el}\\ m_{pl}\\ m_{er}\\ g\end{bmatrix}, \quad X_0 = \begin{bmatrix}x_0\\ q_1\\ q_2\\ q_3\\ q_4\\ q_5\\ u_x\\ u_1\\ u_2\\ u_5\end{bmatrix}. \tag{40}$$

During simulation, the system state $X(t)$ is updated by numerically integrating the dynamic equations from Section 3. At each time step, energy and cable tension are computed:

$$X(t) = \begin{bmatrix} x(t) \\ q_1(t) \\ q_2(t) \\ q_3(t) \\ q_4(t) \\ q_5(t) \\ u_x(t) \\ u_1(t) \\ u_2(t) \\ u_5(t) \end{bmatrix}, \quad E(t) = \begin{bmatrix} T(t) \\ V(t) \end{bmatrix}, \quad T(t) = \begin{bmatrix} T_1(t) \\ T_2(t) \\ T_4(t) \\ T_5(t) \end{bmatrix}, \tag{41}$$

where $T(t)$ and $V(t)$ are the kinetic and potential energies, and T_i are the cable tensions.

All numerical simulations were implemented using Python scientific computing libraries. For Methods 1 and 2, time integration was performed with the `scipy.integrate.solve_ivp` routine, and in Method 2, the dependent variables θ_4 and θ_5 were updated at each step by solving the constraint equations $\bar{f}_h$ using `scipy.optimize.fsolve`. For Method 3, the integration of the reduced differential–algebraic system was carried out using the `scikits.odes.dae` solver. In all cases, the relative and absolute tolerances were set to $rtol = 1 \times 10^{-4}$ and $atol = 1 \times 10^{-6}$, respectively.

4.2. Special Case Simulation and Modeling Insights

To evaluate the robustness of the proposed modeling and simulation framework, we applied all three numerical integration methods (Methods 1–3) to a special case with challenging system parameters, as shown in Figure 6. In this scenario, the system was configured with near-singular cable angles and a mass distribution that accentuated the CKC constraints. For the special configuration, the following parameters were adopted:

- Cable lengths: $l_1 = 30\,\text{m}$, $l_2 = 20\,\text{m}$, $l_3 = 18\,\text{m}$, $l_4 = 20\,\text{m}$, $l_5 = 30\,\text{m}$, $l_0 = 16\,\text{m}$.
- Payload center of gravity: $d = 8\,\text{m}$, $h = 0\,\text{m}$.
- Mass distribution: $m_{ct} = 1000\,\text{ton}$, $m_{el} = 30\,\text{ton}$, $m_{pl} = 300\,\text{ton}$, $m_{er} = 30\,\text{ton}$.
- Initial state: $x = 0$, $\theta_1 = -85^\circ$, $\theta_2 = -80^\circ$, $\theta_3 = 0.782^\circ$, $\theta_4 = 98.269^\circ$, $\theta_5 = 100^\circ$, with all initial velocities set to zero.

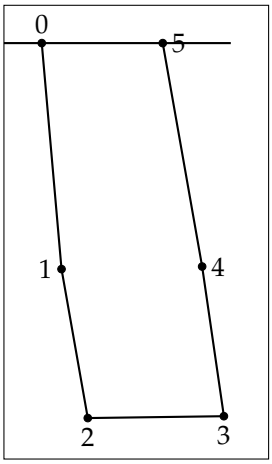


Figure 6. Special case configuration for testing the robustness of the modeling framework.

The simulation results revealed that, under such conditions, constraint drift and numerical instability are more likely to occur, especially when using Method 1 (no constraint correction) or Method 2 (post-step correction). Only Method 3, which embeds the constraints directly into the reduced system, maintained stable and physically consistent results throughout the simulation.

Method 1: No Constraint Correction

In this method, the system is integrated as a differential–algebraic system following Equation (42), without explicitly correcting the position constraints at each integration step. Consequently, the dependent coordinates are not updated to strictly satisfy the CKC constraints during the simulation. As a result, constraint drift may accumulate over time, causing the system to gradually deviate from the ideal CKC configuration. As shown in Figure 7, the distance between nodes 5 and 5′ increases, reflecting a loss of closure in the chain. In particular, the deviation in the $\hat{n}_y$ direction grows from -0.0002 to -0.0015 as the simulation time increases from 10 s to 100 s, with the error increasing nearly 7 times.

$$\begin{cases} \bar{f}_k(\dot{\bar{q}}, \dot{\bar{q}}_r, \bar{u}, \bar{q}, \bar{q}_r, t) = 0 \\ \bar{f}_d(\dot{\bar{u}}, \bar{u}, \bar{q}, \bar{q}_r, t) = 0 \end{cases} \tag{42}$$

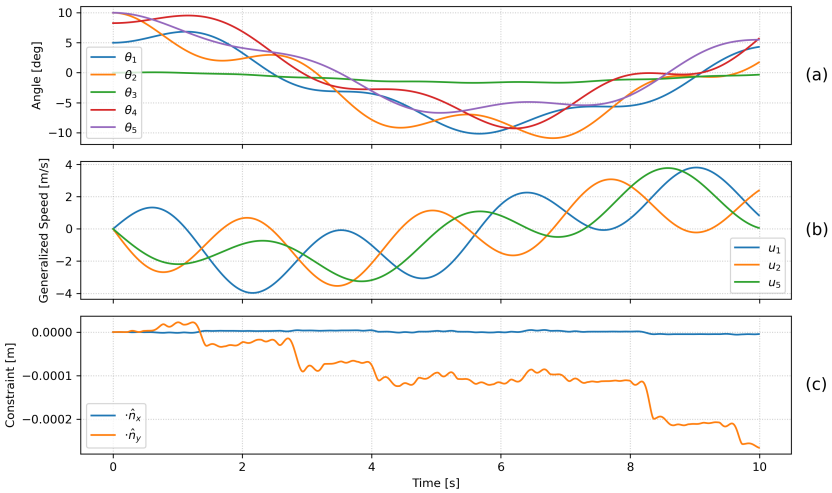


Figure 7. Simulation results without constraint correction for 10 s. (**a**) Angles; (**b**) generalized speeds; (**c**) constraint errors. *Note:* For clarity, all angular variables are plotted with offsets to facilitate comparison of their variations; this convention is maintained in all subsequent figures depicting angular responses.

Method 2: Post-Step Constraint Correction

In this method, the system is integrated as a differential–algebraic system, but after each integration step, the dependent coordinates are adjusted to satisfy the CKC constraints by numerically solving the holonomic equations $\bar{f}_h$ for the dependent variables θ_4 and θ_5. Typically, Method 2 helps maintain the closed-chain structure by projecting the solution back onto the constraint manifold after each integration step. However, in this special case, applying constraint correction introduces significant numerical artifacts. As illustrated in Figure 8, the variables θ_4 and θ_5 display a sawtooth-like linear trend and become coupled, resulting in incorrect behavior. During a 10-second simulation, the maximum error reaches -0.01, and over 100 s, the error increases to -0.3. This indicates that, in certain challenging parameter regimes, post-step constraint correction can lead to substantial numerical errors and instability rather than improving accuracy.

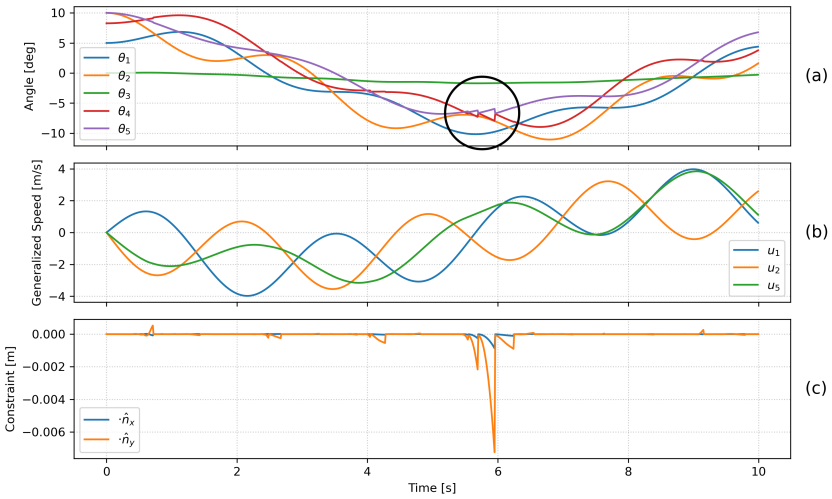


Figure 8. Simulation results with post-step constraint correction for 10 s. (**a**) Angles; (**b**) generalized speeds; (**c**) constraint errors.

Method 3: Reduced System with Embedded Constraints

In this method, two equations corresponding to the non-independent generalized speeds are first eliminated from the system's differential equations, and, instead, the two holonomic constraint equations are directly incorporated, as shown in Equation (43). This reformulation embeds the constraints into the reduced-order system, ensuring that only independent coordinates and speeds are retained. As a result, this method achieves superior computational efficiency, numerical stability, and accuracy. As illustrated in Figure 9, even for a simulation duration of 100 s, the system remains within the prescribed constraint error bounds.

$$\begin{cases} \bar{f}_{k-2}(\dot{\bar{q}}, \bar{u}, \bar{q}, \bar{q}_r, t) = 0 \\ \bar{f}_d(\dot{\bar{u}}, \bar{u}, \bar{q}, \bar{q}_r, t) = 0 \\ \bar{f}_h(\bar{q}, \bar{q}_r, t) = 0 \end{cases} \tag{43}$$

with

$$\bar{f}_{k-2} = \mathbf{M}_{k-2}\dot{\bar{q}} + \bar{g}_{k-2} = 0, \tag{44}$$

where

$$\mathbf{M}_{k-2} = \begin{bmatrix} 1 & 0 & 0 & 0 \\ 0 & l_1 & 0 & 0 \\ 0 & 0 & l_2 & 0 \\ 0 & 0 & 0 & l_5 \end{bmatrix}, \quad \dot{\bar{q}} = \begin{bmatrix} \dot{x} \\ \dot{\theta}_1 \\ \dot{\theta}_2 \\ \dot{\theta}_5 \end{bmatrix}, \quad \bar{g}_{k-2} = \begin{bmatrix} -u_x \\ -u_1 \\ -u_2 \\ -u_5 \end{bmatrix}. \tag{45}$$

Table 4 quantitatively compares the constraint violation errors of the three numerical integration methods. The mean, median, and maximum errors in both the $\hat{n}_x$ and $\hat{n}_y$ directions are reported over the entire simulation. Method 1 (no constraint correction) exhibits moderate constraint drift, with small but persistent errors. Method 2 (post-step constraint correction) results in larger maximum errors and greater variability, indicating numerical artifacts and the occasional loss of constraint satisfaction. Method 3 (reduced system with embedded constraints) achieves the lowest mean and maximum errors, demonstrating superior accuracy and robustness in maintaining closed-chain kinematic constraints.

These results confirm that embedding constraints directly into the reduced system is the most reliable approach for a long-term stable simulation of closed-chain multibody systems. Extensive simulations reveal that the formulation of the dynamic model, especially for closed-chain systems, critically affects computational stability. A detailed analysis of variable selection and numerical stability is provided in the following section.

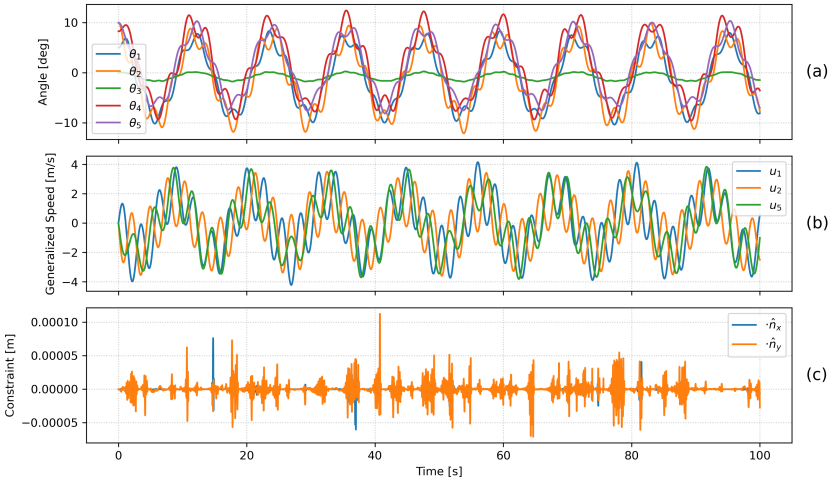


Figure 9. Simulation results with embedded constraints for 100 s. (**a**) Angles; (**b**) generalized speeds; (**c**) constraint errors.

Table 4. Constraint violation statistics of different methods.

	Method 1	**Method 2**	**Method 3**
Constraint Error $\hat{n}_x$			
Mean	1.23×10^{-5}	1.51×10^{-3}	1.49×10^{-6}
Median	1.30×10^{-5}	3.95×10^{-6}	2.92×10^{-7}
Max	2.35×10^{-5}	4.66×10^{-2}	7.64×10^{-5}
Constraint Error $\hat{n}_y$			
Mean	8.55×10^{-4}	1.66×10^{-2}	5.39×10^{-6}
Median	8.66×10^{-4}	6.88×10^{-5}	1.81×10^{-6}
Max	1.68×10^{-3}	3.73×10^{-1}	1.13×10^{-4}

Note: The values presented in this table are averaged from the simulations for 100 s.

4.3. Variable Selection and Numerical Stability

The selection of generalized speeds is critical to ensuring the stability and efficiency of the system simulations. As fundamental variables in Kane's method, generalized speeds play a pivotal role in solving the dynamic equations. According to the constraint equation for the generalized speeds ($\bar{f}_{hs}$), these variables exhibit linear relationships. The Jacobian matrix for any pair of dependent generalized speeds is expressed as

$$J_{hs} = \begin{bmatrix} -\sin\theta_i & -\sin\theta_j \\ \cos\theta_i & \cos\theta_j \end{bmatrix}. \tag{46}$$

where i and j represent the indices of the chosen dependent generalized speeds.

The position constraint equation ($\bar{f}_h$) is nonlinear, although its computational characteristics remain similar. The Jacobian matrix for the generalized coordinates in $\bar{f}_h$ can be represented as

$$J_h = \begin{bmatrix} -l_i \sin\theta_i & -l_j \sin\theta_j \\ l_i \cos\theta_i & l_j \cos\theta_j \end{bmatrix}. \tag{47}$$

The condition numbers of the matrices J_{hs} and J_h provide insight into the numerical stability of their corresponding equations. We systematically compared a wide range of values for these parameters. The results indicate that, under typical engineering conditions where l_i and l_j are of comparable magnitude, their effect on the condition number is negligible. Only when there is an extreme disparity between l_i and l_j does the condition number show a noticeable change. Instead, the angular difference $\theta_i - \theta_j$ plays a dominant

role. Figure 10 shows the variation in the condition number with the angular difference $\theta_i - \theta_j$. The condition number exhibits the following characteristics:

- As $\theta_i - \theta_j \to k\pi$ ($k \in \mathbb{Z}$), the condition number rapidly approaches infinity, indicating singularity within a narrow range.
- Away from these singular points, the condition number decreases significantly, improving the numerical stability.

The singularity condition of the Jacobian matrix can be expressed as

$$\sin(\theta_i - \theta_j) = 0. \tag{48}$$

This condition implies that the Jacobian matrix becomes singular when $\theta_i - \theta_j = k\pi$, where k is an integer.

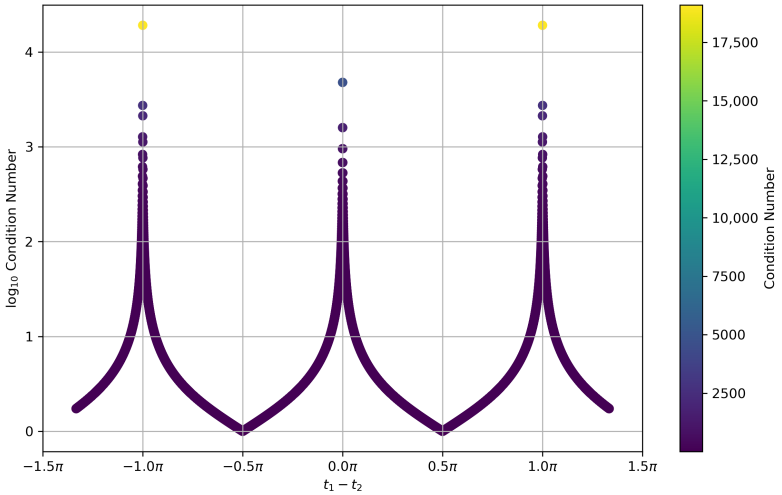


Figure 10. Condition number of the Jacobian matrices J_{hs} and J_h versus angular difference $\theta_i - \theta_j$.

The angular ranges of the generalized coordinates are defined as follows:

- θ_1, θ_2: Typically fluctuate around $-\frac{\pi}{2}$.
- θ_4, θ_5: Typically fluctuate around $\frac{\pi}{2}$.
- θ_3: Generally varies between $-\frac{\pi}{3}$ and $\frac{\pi}{3}$, depending on specific conditions.

When the masses of the equalizer beams (m_{el} and m_{er}) are significantly smaller than the mass of the payload (m_{pl}), the system exhibits single-pendulum-like behavior, where θ_1 and θ_2 (or θ_4 and θ_5) converge, making them unsuitable choices as dependent variable combinations.

These characteristics show that selecting u_3 and another generalized speed as the dependent variables ensures better numerical stability. For generalized coordinates, the same principle applies. Variables closer to the root of the system are used more frequently, whereas end-point variables are preferable as dependent variables to simplify the system equations. For example, choosing u_3 and u_5 should provide simplicity, but additional analysis shows that choosing u_3 and u_4 yields more efficient results, as shown in Table 5, which compares the computational efficiencies of different combinations of dependent variables using the three methods. The results confirm that selecting u_3 and u_4 consistently provides the best balance between stability and efficiency, particularly under Method 3.

Table 5. Comparison of computational efficiency of different configurations.

	Configuration 1			**Configuration 2**		
Dependent Variables	u_4, u_5	u_3, u_5	u_3, u_4	u_4, u_5	u_3, u_5	u_3, u_4
Condition Number	4.479×10^{20}	111.524	108.072	8.260×10^{19}	111.524	108.072
Using Method 1 (s)	7.139	10.567	6.639	8.657	10.857	6.805
Using Method 2 (s)	7.499	11.208	6.999	10.716	11.608	7.005
Using Method 3 (s)	-	7.188	3.659	-	5.790	2.604

Note: Configurations 1 and 2 correspond to the symmetric and asymmetric configurations, which are used and described in Section 5.1. A dash ('-') indicates cases where the computation failed to converge.

For this closed-loop system, the velocity of P_4 can be expressed in two ways:

$$v_4 = u_x \hat{n}_x + u_1 \hat{a}_y + u_2 \hat{b}_y + u_3 \hat{c}_y + u_4 \hat{d}_y, \tag{49}$$

$$v_4 = u_x \hat{n}_x - u_5 \hat{e}_y. \tag{50}$$

Selecting u_4 instead of u_5 as a dependent variable significantly simplifies the description of Point 4's velocity, acceleration, and inertial forces. This simplification reduces the computational complexity and improves the simulation efficiency. This approach is particularly effective for closed-chain systems, where mathematical descriptions of the velocities and accelerations can otherwise become unwieldy. These findings underscore the importance of careful variable selection in complex dynamic modeling.

5. Validation and Model Comparison

This section validates the accuracy of the proposed model by analyzing energy conservation and comparing it with that of traditional simplified models.

5.1. Energy Conservation Analysis

Energy conservation serves as a fundamental criterion for validating the accuracy and physical consistency of multibody dynamic models. In this study, the kinetic energy ($T(t)$) and potential energy ($V(t)$) of the system were computed at each simulation step, and their sum, the total mechanical energy $E(t) = T(t) + V(t)$, was monitored throughout the simulation. For an ideal conservative system, in the absence of external work, the total energy should remain constant over time. To assess the fidelity of the proposed CDPD model, simulations were conducted for both symmetric and asymmetric configurations, with all external control forces set to zero.

For the symmetric configuration, the following parameters were adopted:

- Cable lengths: $l_1 = 30\,\text{m}$, $l_2 = 20\,\text{m}$, $l_3 = 16\,\text{m}$, $l_4 = 20\,\text{m}$, $l_5 = 30\,\text{m}$, $l_0 = 16\,\text{m}$.
- Payload center of gravity: $d = 8\,\text{m}$, $h = 0\,\text{m}$.
- Mass distribution: $m_{ct} = 1000\,\text{ton}$, $m_{el} = 30\,\text{ton}$, $m_{pl} = 300\,\text{ton}$, $m_{er} = 30\,\text{ton}$.
- Initial state: $x = 0$, $\theta_1 = -80^\circ$, $\theta_2 = -80^\circ$, $\theta_3 = 0^\circ$, $\theta_4 = 100^\circ$, $\theta_5 = 100^\circ$, with all initial velocities set to zero.

The initial configuration is illustrated in Figure 11a.

For the asymmetric configuration, the parameters were modified as follows:

- Cable lengths: $l_1 = 30\,\text{m}$, $l_2 = 20\,\text{m}$, $l_3 = 20\,\text{m}$, $l_4 = 8\,\text{m}$, $l_5 = 30\,\text{m}$, $l_0 = 16\,\text{m}$.
- Payload center of gravity: $d = 10\,\text{m}$, $h = 0\,\text{m}$.
- Mass distribution: identical to the symmetric case.
- Initial state: $x = 0$, $\theta_1 = -80^\circ$, $\theta_2 = -80^\circ$, $\theta_3 \approx 38.2^\circ$, $\theta_4 \approx 113.5^\circ$, $\theta_5 = 100^\circ$, with all initial velocities set to zero.

The corresponding initial configuration is shown in Figure 11b.

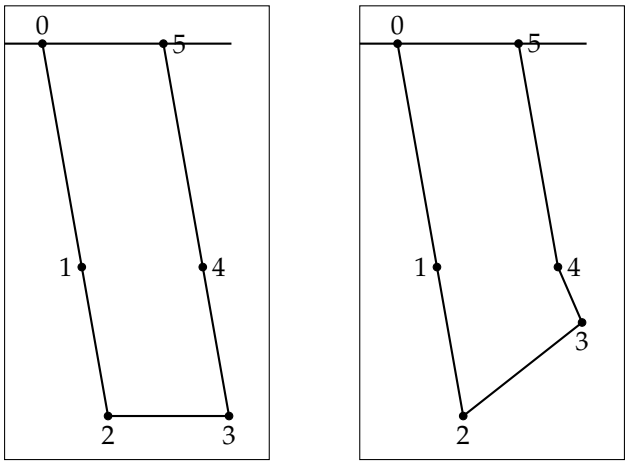


Figure 11. Initial configurations for energy conservation analysis: (**a**) symmetric; (**b**) asymmetric.

The simulation results for both configurations are presented in Figures 12 and 13. In both cases, the total mechanical energy remains constant throughout the simulation, confirming that the CDPD model strictly conserves energy in the absence of external work. For the symmetric configuration, the left and right sides of the system exhibit identical dynamic responses, as expected from the initial symmetry. In contrast, the asymmetric configuration leads to distinct motions on each side, reflecting the influence of structural asymmetry on the system's dynamics.

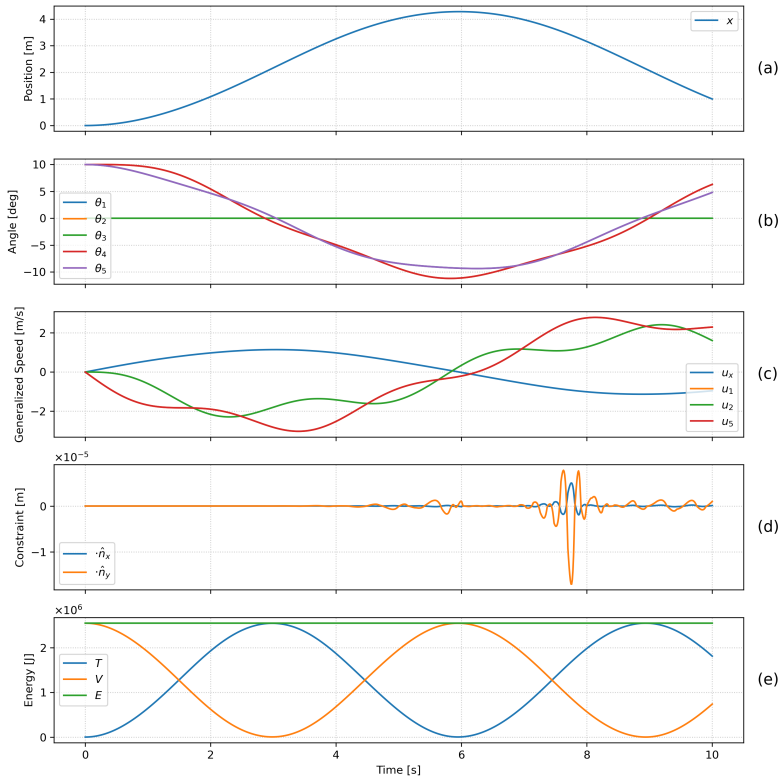


Figure 12. Simulation results for the symmetric configuration: (**a**) cart position; (**b**) angles; (**c**) generalized speeds; (**d**) constraint errors; (**e**) system energy.

In summary, the results demonstrate that the proposed CDPD model is capable of accurately conserving energy and capturing the essential dynamic features of both symmetric and asymmetric gantry crane systems. This provides strong evidence for the

physical validity and numerical robustness of the model, supporting its application to the analysis and control of complex multibody lifting systems.

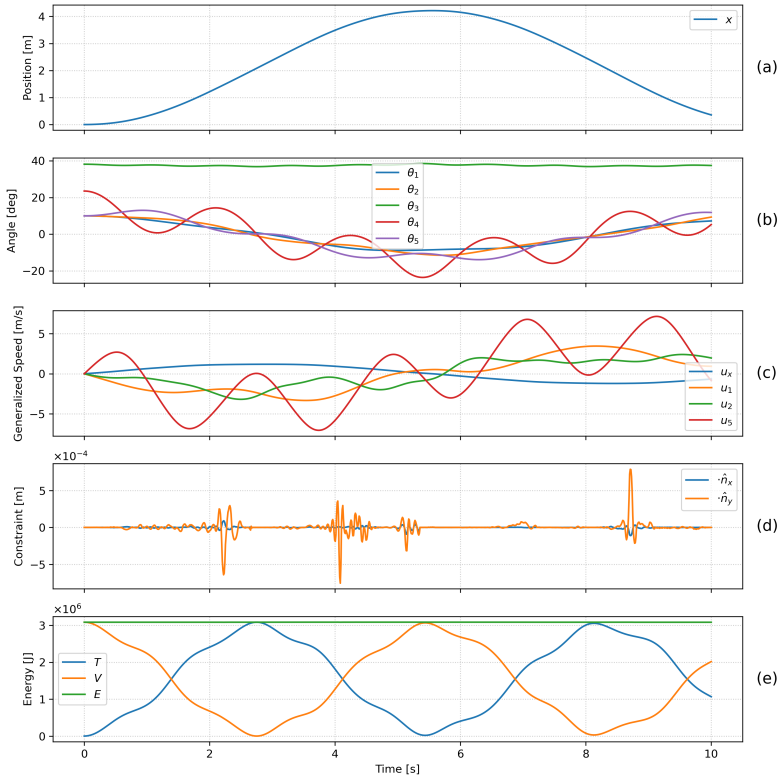


Figure 13. Simulation results for the asymmetric configuration: (**a**) cart position; (**b**) angles; (**c**) generalized speeds; (**d**) constraint errors; (**e**) system energy.

5.2. Comparison with Traditional Models

5.2.1. Model Types and Degeneration

This subsection presents a comparative analysis of four dynamic models: CP, CDP, CPD, and the proposed CDPD. Figure 14 illustrates the structural schematics of each model. The primary distinctions among these models lie in their treatment of pendulum stages and cable configurations. Notably, the CDPD model generalizes the others and can be reduced to any of the simpler forms by imposing appropriate symmetry or parameter constraints.

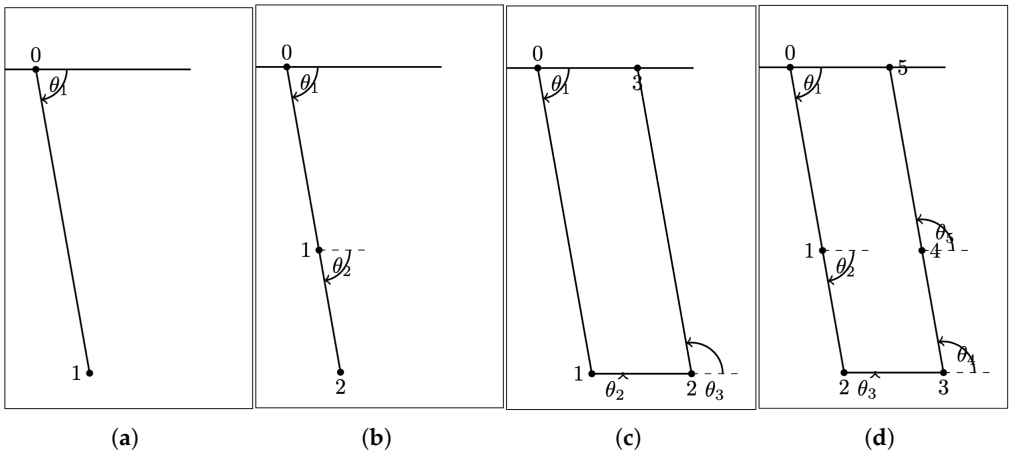


Figure 14. Schematic representations of the initial configurations for cases 1 and 2: (**a**) CP; (**b**) CDP; (**c**) CPD; (**d**) CDPD.

5.2.2. Parameter Mapping

The correspondence between the parameters of the various models is summarized as follows: For the CP model, the effective pendulum length is given by ${}^{CP}l_1 = l_1 + l_2$, while for the CDP model, it is given by ${}^{CDP}l_1 = l_1$ and ${}^{CDP}l_2 = l_2$. In the CPD model, the parameters are mapped as ${}^{CPD}l_1 = l_1 + l_2$, ${}^{CPD}l_2 = l_3$, and ${}^{CPD}l_3 = l_4 + l_5$. The cart mass is consistent across all models, ${}^{CP}m_{ct} = {}^{CDP}m_{ct} = {}^{CPD}m_{ct} = m_{ct}$, as is the payload mass: ${}^{CP}m_{pl} = {}^{CDP}m_{pl} = {}^{CPD}m_{pl} = m_{pl}$. For the CDP model, the equalizer beam mass is given by ${}^{CDP}m_e = m_{el} + m_{er}$. Here, superscripts ^{CP}, ^{CDP}, and ^{CPD} denote the respective model types, while parameters without superscripts refer to the CDPD model.

In the proposed model, the CoG of the payload can be flexibly specified, as illustrated in Figure 4 and Equation (10), to accommodate both the symmetric and asymmetric lifting scenarios encountered in engineering practice. For comparison with traditional models, the CoG is positioned at the midpoint between the two suspension points (nodes 2 and 3), i.e.,

$$d = \frac{l_3}{2}, \quad h = 0, \tag{51}$$

5.2.3. Simulation Scenarios and Results

To further validate the generality and consistency of the proposed CDPD model, a series of numerical simulations were conducted under different parameter regimes. Three representative scenarios were considered: (1) a negligible equalizer beam mass, (2) an increased equalizer beam mass, and (3) asymmetric cable lengths. In each case, the dynamic responses of the CDPD model were compared with those of the traditional models.

Case 1: Negligible Equalizer Beam Mass

In the first scenario, the masses of the equalizer beams were set to $m_{el} = m_{er} = 0.01\, m_{pl}$, effectively rendering their influence negligible relative to the payload. The system was initialized with symmetric cable lengths ($l_1 = l_5 = 30\,\text{m}$, $l_2 = l_4 = 20\,\text{m}$, $l_3 = 16\,\text{m}$), a total cart mass of $m_{ct} = 1000\,\text{ton}$, and a payload mass of $m_{pl} = 300\,\text{ton}$. The initial angles were set to $\theta_1 = \theta_2 = -80^\circ$, $\theta_3 = 0^\circ$, $\theta_4 = \theta_5 = 100^\circ$, with all initial velocities set to zero.

Figure 15 presents the simulation results for this configuration. The coordinate and velocity variables $(x, u_x, \theta_1, \dot{\theta}_1)$ obtained from the CDPD, CP, CPD, and CDP models are nearly indistinguishable, demonstrating that the CDPD model naturally degenerates to the simpler forms when the equalizer beam mass is negligible.

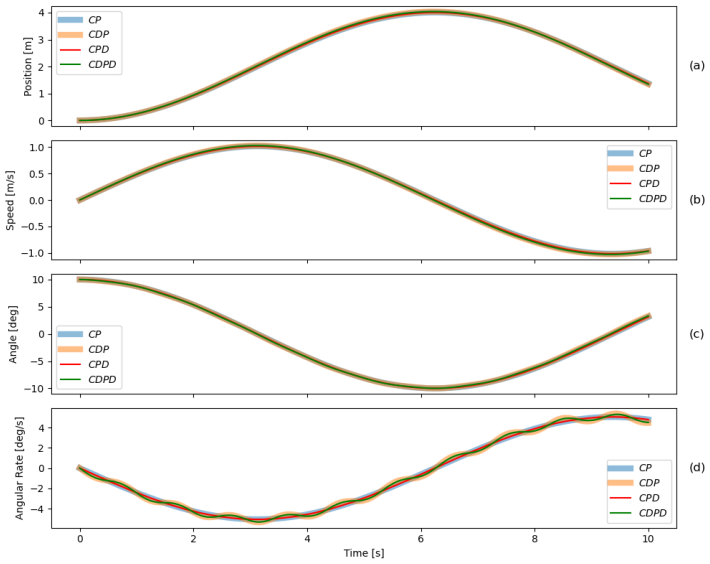


Figure 15. Comparison of coordinate and velocity variables with lightweight equalizer beams: (**a**) cart position; (**b**) cart velocity; (**c**) swing angle θ_1; (**d**) angular velocity $\dot{\theta}_1$.

Case 2: Increased Equalizer Beam Mass

In the second scenario, the equalizer beam masses were increased to $m_{el} = m_{er} = 0.1\, m_{pl}$, while all other parameters remained unchanged. As shown in Figure 16, the dynamic influence of the equalizer beams becomes more pronounced. The CDPD and CDP models yield nearly identical results for the swing angles and angular velocities (see also Figure 17). The CP and CPD models, which neglect double-pendulum effects, deviate from the more complete models as the equalizer beam mass increases.

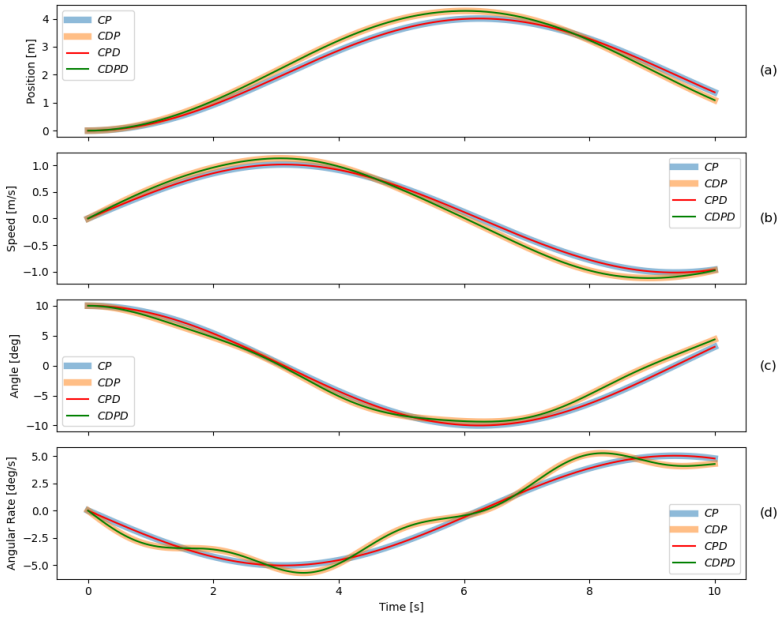


Figure 16. Comparison of coordinate and velocity variables with heavier equalizer beams: (**a**) cart position; (**b**) cart velocity; (**c**) swing angle θ_1; (**d**) angular velocity $\dot{\theta}_1$.

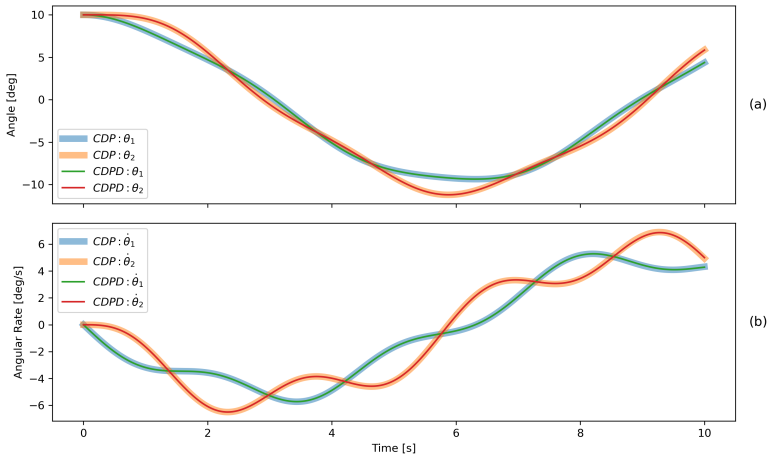


Figure 17. Comparison between CDPD and CDP models for case 2: (**a**) swing angle $\theta_{1,2}$; (**b**) angular velocity $\dot{\theta}_{1,2}$.

Case 3: Asymmetric Cable Lengths

To assess the capability of the CDPD model in handling asymmetric configurations, a third scenario was simulated in which the cable lengths on the two sides were unequal ($l_2 = 20\,\text{m}$, $l_4 = 14.44\,\text{m}$) while maintaining $l_1 = l_5 = 30\,\text{m}$ and $l_3 = 16\,\text{m}$. The equalizer beam masses were set to $m_{el} = m_{er} = 0.01\, m_{pl}$, and the payload's CoG remained at the midpoint between the suspension points. The initial angles and other parameters were the same as in the previous cases.

Figure 18 illustrates schematic representations of the CPD and CDPD models for this configuration. The simulation results, shown in Figure 19, indicate that the dynamic responses of the CDPD and CPD models are nearly identical under these conditions. This demonstrates that the CDPD model can accurately capture the dynamics of systems with unequal cable lengths, and, when the equalizer beam mass is negligible, its response converges to that of the CPD model. Notably, the presence of equalizer beams in the CDPD model introduces small-angle oscillations of the cables during the swinging motion, which are not captured by the CPD model.

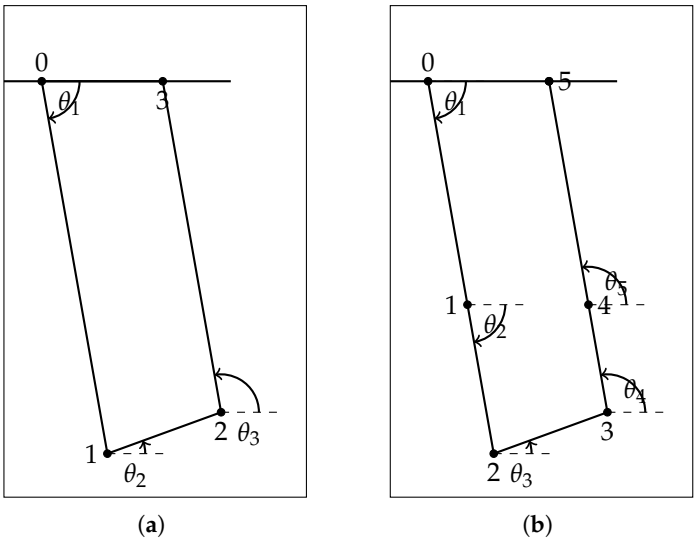


Figure 18. Schematic representations of the initial configurations for case 3: (**a**) CPD; (**b**) CDPD.

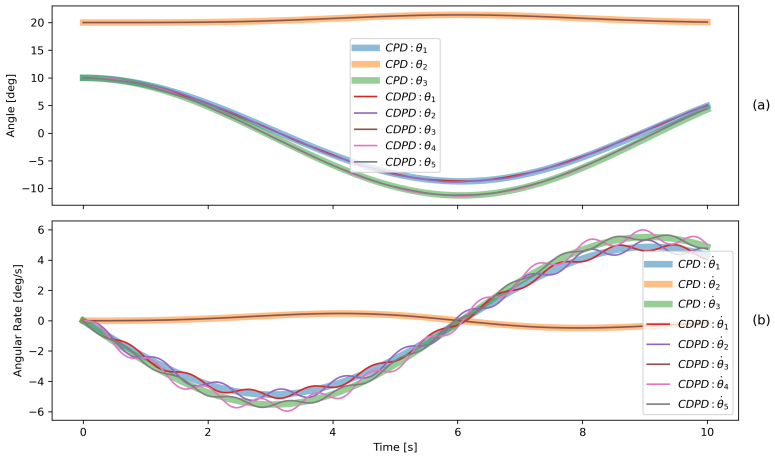


Figure 19. Comparison between CDPD and CPD models for case 3: (**a**) angles; (**b**) angular velocities.

5.3. Summary

The validation and comparison analyses confirmed that the proposed CDPD model is both accurate and versatile. The model strictly conserves energy in all tested scenarios, confirming its physical consistency. When the CDPD system configurations approach symmetry and the equalizer beam mass is negligibly small, the CDPD model's responses align closely with those of simpler models. As the equalizer beam mass increases, the CDPD model is only close to the CDPD model, while the CP and CDP models diverge significantly. For the asymmetric configurations, the CDPD model with a negligible equalizer mass also matches the CPD model's responses, while the CDP model fails to capture the dynamics accurately, such as the small-angle oscillations of the cables during swinging motions. As

the beam mass increases or cable asymmetry is introduced, the CDPD model captures dynamic effects that conventional models cannot. These results establish the CDPD model as a unified and robust framework for simulating and analyzing complex gantry crane systems with varying configurations.

6. Case Studies

This section analyzes the effects of special hoisting parameters on the dynamic response of the CDPD system, focusing on scenarios that deviate from standard symmetric configurations. Such cases are common in practical engineering, where the payload geometry, suspension point arrangement, or operational constraints introduce asymmetries or non-vertical cable orientations.

6.1. Discrete PID Control Algorithm

The discrete PID controller is a widely used feedback control algorithm in industrial applications. It computes the control input at each sampling instant based on the current, past, and accumulated errors between the desired reference and the measured output.

The discrete PID control law can be expressed as

$$F[k] = K_p\, e[k] + K_i \sum_{i=0}^{k} e[i]\, T_s + K_d\, \frac{e[k] - e[k-1]}{T_s} \tag{52}$$

where:

- $F[k]$: The control input at the k-th sampling instant; in this study, it represents the horizontal control force F_C applied to the crane cart.
- $e[k] = r[k] - y[k]$: The error between the reference value $r[k]$ and the measured output $y[k]$; here, $r[k]$ is the target position of the cart, and $y[k]$ is the current cart position x.
- K_p, K_i, K_d: The proportional, integral, and derivative gain coefficients, respectively.
- T_s: The sampling period.

The proportional term reacts to the current error, the integral term accumulates past errors to eliminate steady-state offset, and the derivative term predicts future error trends to improve response speed and stability. In practical digital implementations, the integral and derivative actions are computed using finite sums and differences, and anti-windup or filtering techniques may be applied to enhance robustness.

6.2. Hoisting with Unequal Suspension Heights

In shipbuilding, hoisting operations often involve subassemblies with diverse shapes and weight distributions. Standard double-pendulum models are insufficient to accurately simulate such configurations, especially for asymmetrical systems. A common scenario involves L-shaped or triangular subassemblies, such as bow or stern sections, sloped decks, or bulkhead corner segments—where the structure is triangular or trapezoidal and the suspension points are located at different heights, resulting in unequal cable lengths. These complexities necessitate a more comprehensive model for reliable analysis.

This section considers a hoisting system where the equalizer beams on both sides have identical weights, isolating the impact of height differences. The system configuration is depicted in Figure 20. The parameters for this system are set as follows:

- Simulation time: 200 s.
- Cable lengths: $l_1 = 30\,\text{m}$, $l_2 = 20\,\text{m}$, $l_3 = 20\,\text{m}$, $l_4 = 20\,\text{m}$, $l_5 = 18\,\text{m}$, $l_0 = 16\,\text{m}$.
- Mass parameters: $m_{ct} = 1000\,\text{t}$, $m_{el} = m_{er} = 30\,\text{t}$, $m_{pl} = 600\,\text{t}$.
- Initial conditions: $x = 0$, $\theta_1 = \theta_2 = -90^\circ$, $\theta_3 = 36.87^\circ$, $\theta_4 = \theta_5 = 90^\circ$; all initial velocities are zero.

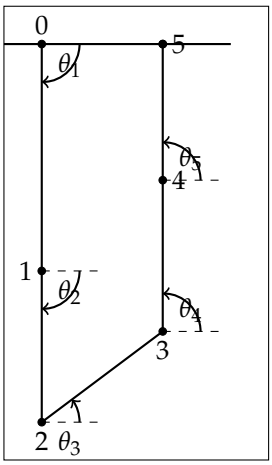


Figure 20. Schematic of a hoisting system with unequal suspension heights.

The CDPD model was implemented in a numerical simulation environment, and the discrete PID control algorithm was applied to regulate the cart's position. The control gains were set as follows: $K_p = 1000$, $K_i = 10$, and $K_d = 50$. The sampling period was set to $T_s = 0.01$ s. The goal of the control was to move the cart to a target position of $x = 20$ m while maintaining stability in the swinging motion of the cables.

6.3. Simulation Result

The simulation results demonstrate that the CDPD model effectively captures the dynamic behavior of the hoisting system, including the influence of unequal suspension heights on the cart's motion and the oscillatory behavior of the suspended payload.

The results are presented in Figure 21, which shows that the cart smoothly moves from its initial position of 0 m to the target position of 20 m, achieving accurate positioning. The velocity profile exhibits fluctuations during the acceleration and deceleration phases, primarily due to the swinging effects of the suspended payload. The control force, presented in Figure 22a, also shows similar fluctuations during these phases, reflecting the coupled dynamics of the system. Figure 21c,d show the angles and angular velocities of the cables, which indicate that the PID control effectively suppresses large swings, leading to a stable final state.

Figure 22a illustrates the time history of the control force (a) throughout the hoisting process. The control force exhibits a rapid increase at the initial stage to accelerate the cart, followed by a gradual decrease and stabilization as the system approaches the target position. Figure 22b shows that the proportional, integral, and derivative components reflect the influence of the instantaneous error, accumulated error, and error rate of change on the control action, respectively. It should be noted that the derivative term dampens oscillations by predicting future errors based on the rate of error change, which corresponds to the cart's speed, as shown in Figure 21b.

Figure 23 illustrates the time histories of the four cable tensions (T_1, T_2, T_4, and T_5) throughout the PID-controlled hoisting process. Figure 23a presents the time-domain curves for all cable tensions, showing a pronounced initial jump followed by rapid oscillatory decay and eventual stabilization. Figure 23b displays the tensions in the upper cables (T_1 and T_5), with the red dashed line indicating the reference level ($W_{pl}/2 + W_{eq}$). Figure 23c compares the tensions in the lower cables (T_2 and T_4), with the orange dashed line marking the half-payload weight ($W_{pl}/2$) reference.

It can be observed that the tensions on the left and right sides remain nearly identical and symmetrically distributed throughout the process. The fluctuations in tension are primarily attributed to the swinging motion of the payload, which affects the instantaneous

weight distribution. The slight differences in the amplitude of the fluctuations between the left and right cables arise from disparities in the cable lengths and the combined effects of centripetal forces. Overall, the trends in cable tension are consistent with theoretical expectations, confirming that the model accurately captures the force transmission and load-sharing characteristics of the cables under PID control.

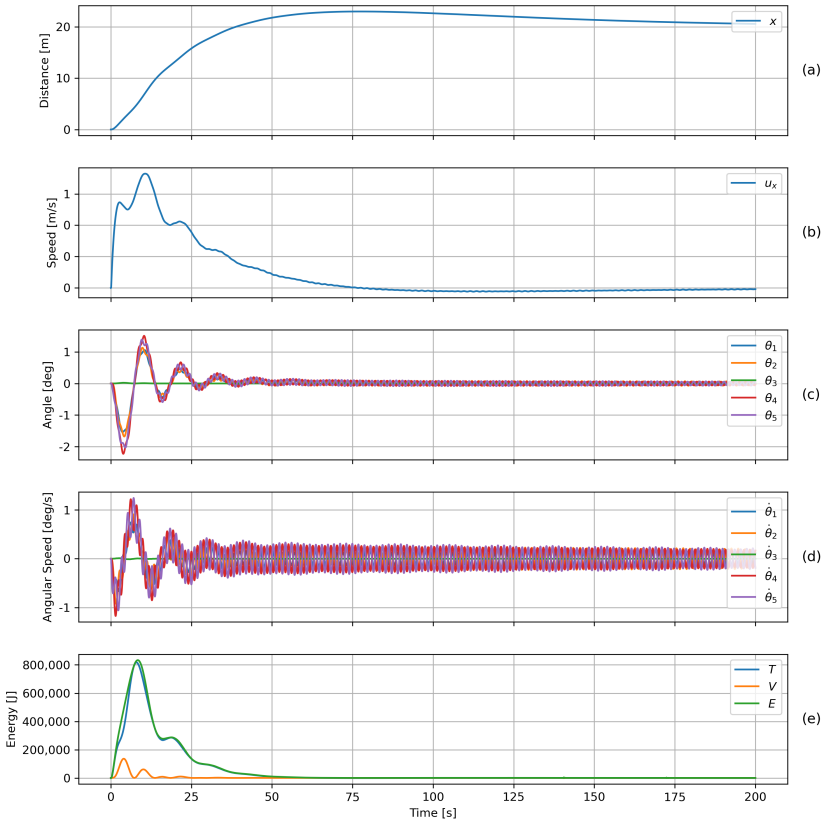


Figure 21. Simulation results with PID control: (**a**) cart position; (**b**) cart velocity; (**c**) swing angles; (**d**) angular velocity; (**e**) system energy.

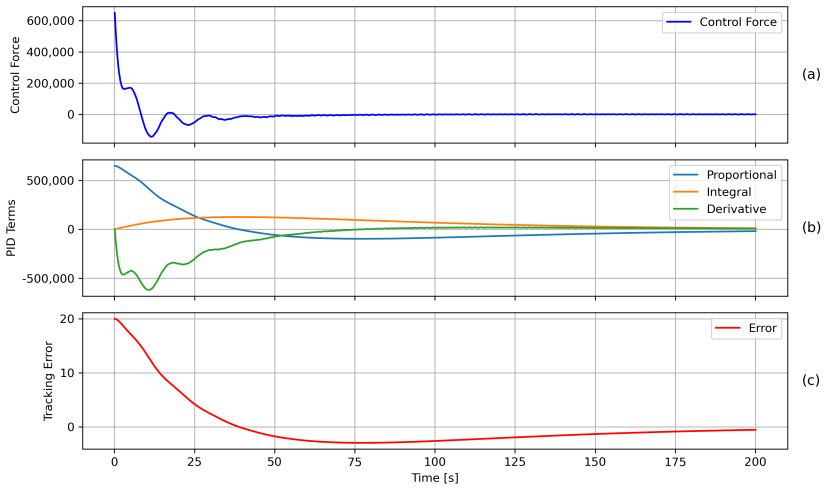


Figure 22. Time history of PID control terms: (**a**) control force; (**b**) PID terms; (**c**) tracking error.

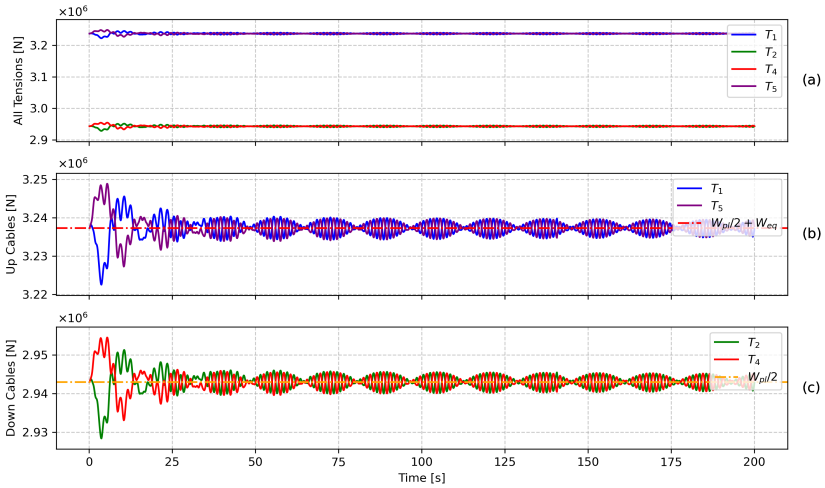


Figure 23. Time histories of cable tensions T_i ($i = 1, 2, 4, 5$): (**a**) all tensions; (**b**) T_1 and T_5; (**c**) T_2 and T_4.

7. Conclusions

This study presents a unified dynamic modeling framework for large-scale gantry crane systems, termed the CDPD model. By systematically incorporating dual-cable and double-pendulum effects, equalizer beam mass, and CKC constraints, the proposed model addresses the limitations of traditional single- and double-pendulum approaches and enables an accurate simulation of complex lifting scenarios.

The main contributions of this work are as follows:

- The explicit consideration of the equalizer beam mass and closed-chain constraints, which are critical for accurate force transmission and load sharing in practical engineering applications;
- The formulation of a unified dynamic model based on Kane's method, with the systematic selection of independent and dependent variables to achieve a concise and numerically stable set of equations suitable for complex hoisting scenarios.

Simulation and comparative analyses confirm that the CDPD model strictly conserves energy and maintains dynamic consistency in both symmetric and asymmetric configurations. Case studies demonstrate the model's extensible structure, which supports the integration of advanced control strategies, proving it suitable for real-world engineering scenarios.

It should be noted that the current formulation assumes rigid bodies and massless, inextensible cables, and it does not account for out-of-plane dynamics or certain external disturbances. Future work will focus on relaxing these assumptions and incorporating cable flexibility, three-dimensional effects, and experimental validation to further enhance the model's fidelity and practical value.

Author Contributions: Conceptualization, methodology, formal analysis, investigation, software development, writing—original draft, and project supervision, B.J.; supervision, data curation, software implementation, validation, and writing—review and editing, J.Z.; investigation, resources, visualization, and manuscript preparation, P.G.; software development, formal analysis, validation, and visualization, H.Z.; methodology refinement and writing—review and editing, S.G. All authors have read and agreed to the published version of the manuscript.

Funding: This research received no external funding.

Data Availability Statement: The original contributions presented in this study are included in the article. Further inquiries can be directed to the corresponding author(s).

Acknowledgments: The authors would like to express their sincere gratitude to all individuals and institutions who contributed to the successful completion of this research. We acknowledge the valuable insights and constructive feedback provided by the anonymous reviewers, which significantly improved the quality and clarity of this manuscript.

Conflicts of Interest: The authors declare no conflicts of interest.

Abbreviations

The following abbreviations are used in this manuscript:

CDPD	Cart double pendulum with dual cables
CKC	Closed kinematic chain
CP	Cart pendulum
CPD	Cart pendulum with dual cables
CDP	Cart double pendulum
PID	Proportional–integral–derivative (controller)
ODEs	Ordinary differential equations
CoG	Center of gravity
DAEs	Differential–algebraic equations
SMC	Sliding mode control

References

1. Abdel-Rahman, E.M.; Nayfeh, A.H.; Masoud, Z.N. Dynamics and Control of Cranes: A Review. *J. Vib. Control* **2003**, *9*, 863–908. [CrossRef]
2. Ramli, L.; Mohamed, Z.; Abdullahi, A.M.; Jaafar, H.I.; Lazim, I.M. Control strategies for crane systems: A comprehensive review. *Mech. Syst. Signal Process.* **2017**, *95*, 1–23. [CrossRef]
3. Hong, K.S.; Shah, U.H. *Dynamics and Control of Industrial Cranes*; Springer: Berlin/Heidelberg, Germany, 2019.
4. Muddassir, M.; Zayed, T.; Ali, A.H.; Elrifaee, M.; Abdulai, S.F.; Yang, T.; Eldemiry, A. Automation in tower cranes over the past two decades (2003–2024). *Autom. Constr.* **2025**, *170*, 105889. [CrossRef]
5. Mojallizadeh, M.R.; Brogliato, B.; Prieur, C. Modeling and control of overhead cranes: A tutorial overview and perspectives. *Annu. Rev. Control* **2023**, *56*, 100877. [CrossRef]
6. Kim, G.H.; Yoon, M.; Jeon, J.Y.; Hong, K.S. Data-driven Modeling and Adaptive Predictive Anti-swing Control of Overhead Cranes. *Int. J. Control. Autom. Syst.* **2022**, *20*, 2712–2723. [CrossRef]
7. Liu, Z.; Wang, S.; Chen, H.; Li, G.; Zhang, H. Dynamic Modeling and Anti-swing Control of Double Pendulum Payload System of Overhead Crane. In Proceedings of the 2022 IEEE 17th International Conference on Control & Automation (ICCA), Naples, Italy , 27–30 June 2022. [CrossRef]
8. Fatehi, M.H.; Eghtesad, M.; Necsulescu, D.S.; Fatehi, A.A. Tracking control design for a multi-degree underactuated flexible-cable overhead crane system with large swing angle based on singular perturbation method and an energy-shaping technique. *J. Vib. Control* **2019**, *25*, 1752–1767. [CrossRef]
9. Rome, T.; Adams, C.; Singhose, W. Dynamic Model for Improved Controller Design in Tower Crane Disassembly. In Proceedings of the 2024 IEEE International Conference on Advanced Intelligent Mechatronics (AIM), Boston, MA, USA, 15–19 July 2024; pp. 1118–1125. [CrossRef]
10. Shi, H.; Yao, F.; Yuan, Z.; Tong, S.; Tang, Y.; Han, G. Research on nonlinear coupled tracking controller for double pendulum gantry cranes with load hoisting/lowering. *Nonlinear Dyn.* **2022**, *108*, 223–238. [CrossRef]
11. Chen, Q.; Cheng, W.; Liu, J.; Du, R. Partial state feedback sliding mode control for double-pendulum overhead cranes with unknown disturbances. *Proc. Inst. Mech. Eng. Part J. Mech. Eng. Sci.* **2022**, *236*, 3902–3911. [CrossRef]
12. Rigatos, G. Nonlinear Optimal Control for the Underactuated Double-Pendulum Overhead Crane. *J. Vib. Eng. Technol.* **2023**, *12*, 1203–1223. [CrossRef]
13. Tuan, L.A.; Lee, S.G. Sliding mode controls of double-pendulum crane systems. *J. Mech. Sci. Technol.* **2013**, *27*, 1863–1873. [CrossRef]
14. Wang, J.; Liu, K.; Wang, S.; Chen, H.; Sun, Y.; Niu, A.; Li, H. Dynamic Analysis and Experiment of Underactuated Double-Pendulum Anti-Swing Device for Ship-Mounted Jib Cranes. *Pol. Marit. Res.* **2022**, *29*, 145–154. [CrossRef]
15. Miao, X.; Zheng, S.; Ouyang, H. Fault-tolerant controller design for tower cranes considering distributed payload beams. *Int. J. Robust Nonlinear Control* **2023**, *34*, 3516–3547. [CrossRef]

16. Li, Z.; Ma, X.; Li, Y. Nonlinear partially saturated control of a double pendulum offshore crane based on fractional-order disturbance observer. *Autom. Constr.* **2022**, *137*, 104212. [CrossRef]
17. Guo, Q.; Chai, L.; Liu, H. Anti-swing sliding mode control of three-dimensional double pendulum overhead cranes based on extended state observer. *Nonlinear Dyn.* **2022**, *111*, 391–410. [CrossRef]
18. Maleki, E.; Singhose, W.; Hawke, J.; Vaughan, J. Dynamic Response of a Dual-Hoist Bridge Crane. In Proceedings of the ASME 2013 Dynamic Systems and Control Conference, V003T48A002, Palo Alto, CA, USA, 21–23 October 2013; Volume 3. [CrossRef]
19. Arena, A.; Casalotti, A.; Lacarbonara, W.; Cartmell, M.P. Three-Dimensional Modeling of Container Cranes. In Proceedings of the ASME 2013 International Design Engineering Technical Conferences and Computers and Information in Engineering Conference, V07AT10A069, Portland, OR, USA, 4–7 August 2013; Volume 7A. [CrossRef]
20. Arena, A.; Casalotti, A.; Lacarbonara, W.; Cartmell, M.P. Dynamics of container cranes: Three-dimensional modeling, full-scale experiments, and identification. *Int. J. Mech. Sci.* **2015**, *93*, 8–21. [CrossRef]
21. Lu, B.; Fang, Y.; Sun, N. Modeling and verification for a four-rope crane. In Proceedings of the 2015 IEEE International Conference on Cyber Technology in Automation, Control, and Intelligent Systems (CYBER), Shenyang, China, 8–12 June 2015. [CrossRef]
22. Lu, B.; Fang, Y.; Sun, N. Adaptive trajectory tracking control for a four-rope crane. In Proceedings of the 2015 IEEE International Conference on Advanced Intelligent Mechatronics (AIM), Busan, Republic of Korea, 7–11 July 2015. [CrossRef]
23. Lu, B.; Fang, Y.; Sun, N. Nonlinear control for underactuated multi-rope cranes: Modeling, theoretical design and hardware experiments. *Control Eng. Pract.* **2018**, *76*, 123–132. [CrossRef]
24. Lu, B.; Fang, Y.; Sun, N. Adaptive Output-Feedback Control for Dual Overhead Crane System With Enhanced Anti-Swing Performance. *IEEE Trans. Control Syst. Technol.* **2020**, *28*, 2235–2248. [CrossRef]
25. Wen, T.; Fang, Y.; Lu, B. Neural network-based adaptive sliding mode control for underactuated dual overhead cranes suffering from matched and unmatched disturbances. *Auton. Intell. Syst.* **2022**, *2*, 1. [CrossRef]
26. Leban, F.A.; Diaz-Gonzalez, J.; Parker, G.G.; Zhao, W. Inverse Kinematic Control of a Dual Crane System Experiencing Base Motion. *IEEE Trans. Control Syst. Technol.* **2015**, *23*, 331–339. [CrossRef]
27. Fu, Y.; Yang, T.; Sun, N.; Zhang, J.; Fang, Y. Dynamics modeling and analysis for cooperative dual rotary crane systems. In Proceedings of the 2018 37th Chinese Control Conference (CCC), Wuhan, China, 25–27 July 2018; pp. 5492–5497.
28. Sun, N.; Yang, T.; Fang, Y.; Lu, B.; Qian, Y. Nonlinear Motion Control of Underactuated Three-Dimensional Boom Cranes With Hardware Experiments. *IEEE Trans. Ind. Inform.* **2018**, *14*, 887–897. [CrossRef]
29. Sun, N.; Fu, Y.; Yang, T.; Zhang, J.; Fang, Y.; Xin, X. Nonlinear Motion Control of Complicated Dual Rotary Crane Systems Without Velocity Feedback: Design, Analysis, and Hardware Experiments. *IEEE Trans. Autom. Sci. Eng.* **2020**, *17*, 1017–1029. [CrossRef]
30. Liu, Z.; Fu, Y.; Sun, N.; Yang, T.; Fang, Y. Collaborative Antiswing Hoisting Control for Dual Rotary Cranes With Motion Constraints. *IEEE Trans. Ind. Inform.* **2022**, *18*, 6120–6130. [CrossRef]
31. Zhao, X.; Huang, J. Distributed-mass payload dynamics and control of dual cranes undergoing planar motions. *Mech. Syst. Signal Process.* **2019**, *126*, 636–648. [CrossRef]
32. Huang, J.; Zhu, K. Dynamics and control of three-dimensional dual cranes transporting a bulky payload. *Proc. Inst. Mech. Eng. Part J. Mech. Eng. Sci.* **2020**, *235*, 1956 – 1965. [CrossRef]
33. Feng, X.; Yang, T.; Zhang, T.; Wang, J.; Pang, R.; Chen, X.; Wu, Q.; Sun, N. Dynamic Modeling of Variable-Length Dual Cable Boom Cranes with Postural Adjustments. In Proceedings of the International Conference on Guidance, Navigation and Control, Changsha, China, 9–11 August 2024; Springer: Singapore, 2024; pp. 140–151.
34. Sarkar, S.; Fitzgerald, B. Use of Kane's Method for Multi-Body Dynamic Modelling and Control of Spar-Type Floating Offshore Wind Turbines. *Energies* **2021**, *14*, 6635. [CrossRef]
35. Qiu, S.; Ren, H.; Li, H.; Zhou, Y.; Wang, D. Multibody Dynamics Model and Simulation for the Totally Enclosed Lifeboat Lowered From Ship in Rough Seas. *IEEE Access* **2021**, *9*, 32171–32187. [CrossRef]
36. Zhong, Y.; Wang, L. A Method to Establish the Dynamic Models of Multibody System Based on Kane's Equations. In Proceedings of the the 2nd International Conference on Modelling, Identification and Control, Paris, France, 9–10 August 2015; Atlantis Press: Dordrecht, The Netherlands, 2015; pp. 21–26. [CrossRef]
37. Marques, F.; Roupa, I.; Silva, M.T.; Flores, P.; Lankarani, H.M. Examination and comparison of different methods to model closed loop kinematic chains using Lagrangian formulation with cut joint, clearance joint constraint and elastic joint approaches. *Mech. Mach. Theory* **2021**, *160*, 104294. [CrossRef]
38. Wang, Z.; Ghorbel, F.H. Modeling Closed Kinematic Chains for Control: A Comparative Study. In Proceedings of the ASME 2005 International Mechanical Engineering Congress and Exposition, Orlando, FL, USA, 5–11 November 2005. [CrossRef]
39. Zahedi, A.; Shafei, A.M.; Shamsi, M. On the dynamics of multi-closed-chain robotic mechanisms. *Int. J. Non-Linear Mech.* **2022**, *147*, 104241. [CrossRef]

40. Kane, T.R.; Levinson, D.A. *Dynamics, Theory and Applications*; McGraw Hill: New York, NY, USA, 1985.
41. Vallery, H.; Schwab, A.L. *Advanced Dynamics*; Delft University of Technology: Delft, The Netherlands, 2017.

Disclaimer/Publisher's Note: The statements, opinions and data contained in all publications are solely those of the individual author(s) and contributor(s) and not of MDPI and/or the editor(s). MDPI and/or the editor(s) disclaim responsibility for any injury to people or property resulting from any ideas, methods, instructions or products referred to in the content.